Supplementary Information

Table 1 Data collection, phasing and refinement statistics

	Native	Pt1	Pt2
Data collection			
Space group	$P6_3$	$P6_3$	$P6_3$
Cell dimensions			
a, *c* (Å)	119.72, 83.14	119.12, 83.15	124.51, 88.36
α, β, γ (°)	90, 90, 120	90, 90, 120	90, 90, 120
			Peak
Wavelength (Å)	1.062	1.062	1.070
$I/\sigma I$	34.7 (2.2)	26.1 (3.2)	26.2 (3.0)
Completeness (%)	99.6 (98.3)	99.8 (100)	99.9 (99.2)
Redundancy	7.9 (5.8)	7.6 (6.1)	18.4 (10.6)
Phasing		SIRAS	SAD
Figure of merit (resolution)		0.34 (40-5.0 Å)	0.35 (40-4.0 Å)
Refinement			
Resolution (Å)	28.8-2.44 (2.48-2.44) *		
No. reflections	49037		
R_{work}/ R_{free} §	19.6/22.8		
No. atoms	3070		
Protein	2951		
Uridine/Na^+/detergent	17/1/58		
Water	43		
B-factors **(**Å^2)			
Protein	58.2		
Uridine/Na^+/detergent	43.7/48.5/69.3		
Water	52.9		
R.m.s deviations			
Bond lengths (Å)	0.007		
Bond angles (°)	0.94		

*Highest resolution shell is shown in parenthesis.

§5% of the data that were excluded from refinement were used in the R_{free} calculation.

Supplementary Methods

Radioactive flux experiments: Flux experiments at varied sodium concentrations were done by including appropriate concentrations of choline chloride in the outside buffer to maintain a consistent ionic strength for all experiments (i.e. for 20 mM NaCl, 80 mM choline chloride was also included).

Electrogenicity experiments were done using the following conditions: 200 mM KCl, 100 mM choline chloride, and 20 mM HEPES pH 7.4 were included inside the vesicles, and 280 mM choline chloride, 20 mM NaCl, and 20 mM HEPES pH 7.4 were included outside the vesicles. These conditions result in a negative-inside membrane potential in the presence of valinomycin due to outward K^+ flux. Flux was initiated and measured after the addition of 2.3 μM [5,6-^{3}H]-uridine in the presence of and in the absence of 1 μM valinomycin.

Flux experiments at varied pH values were done in the absence of sodium (NaCl replaced with 100 mM choline chloride). At pH 5.5 and pH 6.5, 20 mM MES was used in the outside buffer instead of HEPES. Dilution of the reconstitution buffer (100 mM choline chloride, 200 mM KCl, and 20 mM HEPES pH 7.4) by 20-fold into the outside buffer (100 mM choline chloride, 200 mM KCl, 20 mM MES pH 5.5 or 6.5) resulted in solutions with pH values very close to those of the outside buffers (5.5 or 6.5).

Cross-linking experiments: For each cross-linking experiment, 50 μM $CuSO_4$ and 150 μM of 1,10-phenanthroline were added and allowed to incubate at room temperature for 20 min. The reactions were quenched by the addition of 20 μM *N*-ethylmaleimide (NEM) and 50 mM EDTA. NEM was also added to air-oxidized samples to block further oxidation during SDS-PAGE.

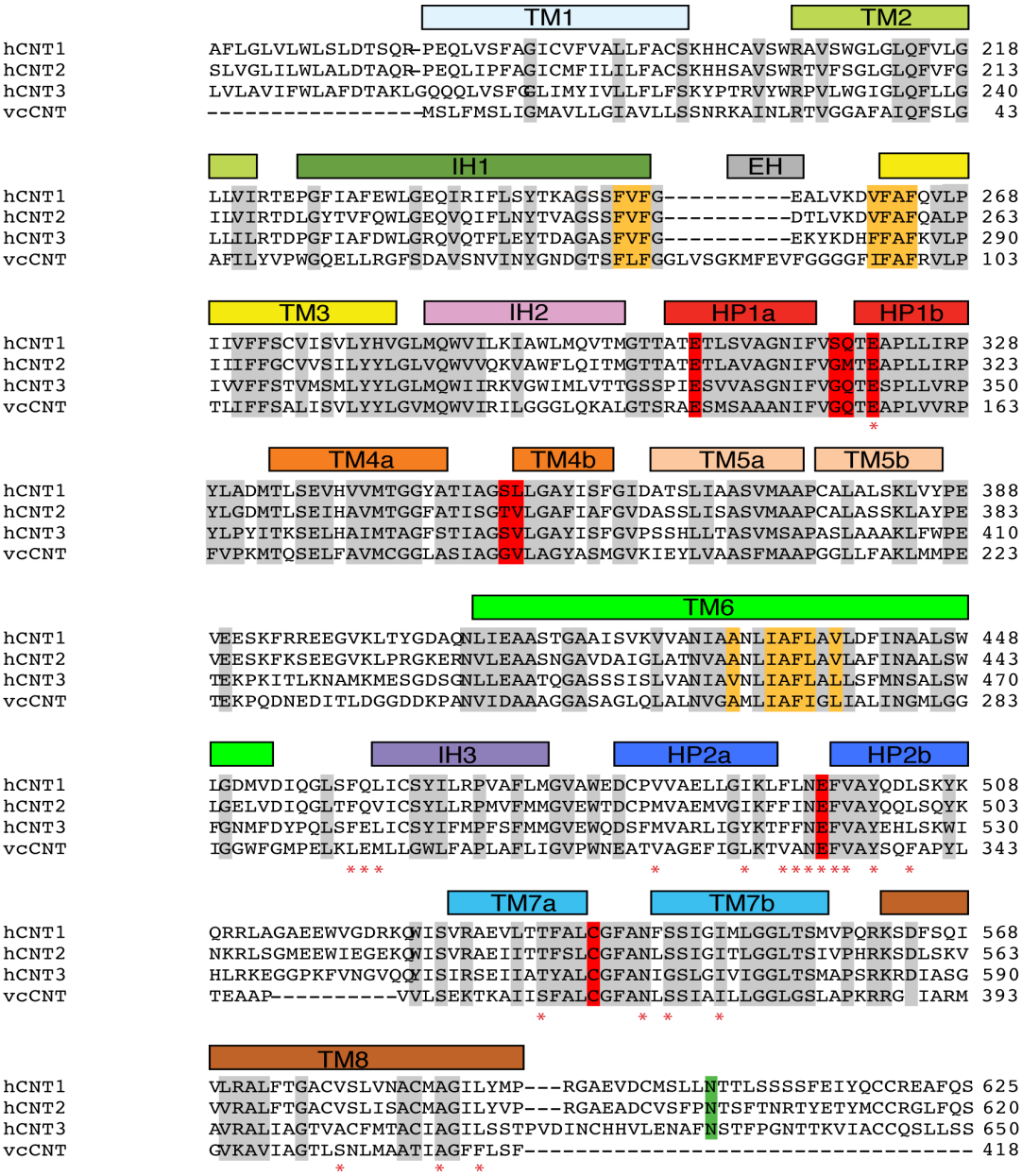

Supplementary Figure 1. Sequence alignment of hCNT1 (NP_004204.3), hCNT2 (NP_004203.2), hCNT3 (NP_071410.1), and vcCNT (NP_231982.1). Bars representing helices are color-coded with the same scheme as Figures 3 and 5. Conserved residues are highlighted in grey, functionally important residues are highlighted in red, and conserved residues that are involved in trimerization are highlighted in yellow. Residues that are accessible to the extracellular side when mutated to cysteines [1] are marked with red asterisks. Glycosylation site is highlighted in green [2].

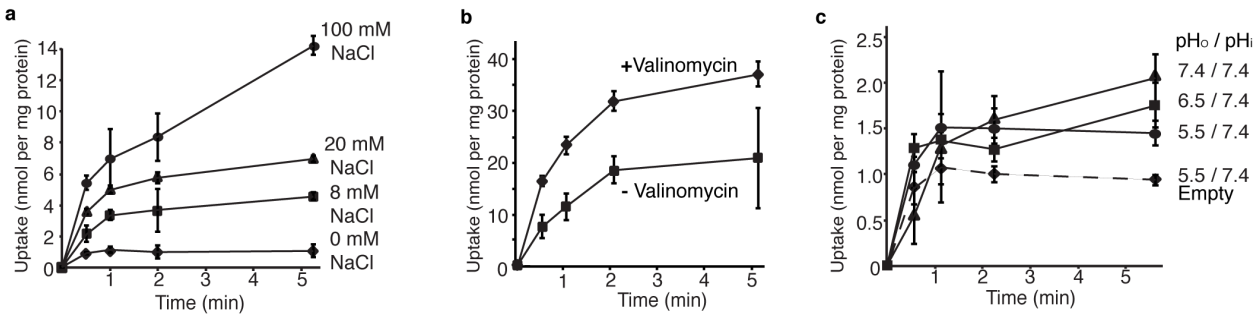

Supplementary Figure 2. vcCNT-mediated nucleoside transport is Na^+-dependent and electrogenic. **a**, Time course of the uptake of 2.4 µM [5,6-^{3}H]-uridine into vesicles containing vcCNT in the presence of various sodium gradients (circles: 100 mM NaCl, triangles: 20 mM NaCl, squares: 8 mM NaCl, diamonds: no NaCl). **b**, Time course of the uptake of 2.3 µM [5,6-^{3}H]-uridine into vesicles containing vcCNT with (diamonds) and without (squares) valinomycin in the presence of 20 mM NaCl. **c,** Time course of the uptake of 2.4 µM [5,6-^{3}H]-uridine into vesicles containing vcCNT at various pH gradients [pH_{out}/pH_{in} = 7.4/7.4 (triangles), 6.5/7.4 (squares), 5.5/7.4 (circles), and empty vesicles at 5.5/7.4 (diamonds)] in the absence of a sodium gradient. Note the difference in scale compared to **a** (in the presence of a Na^+ gradient).

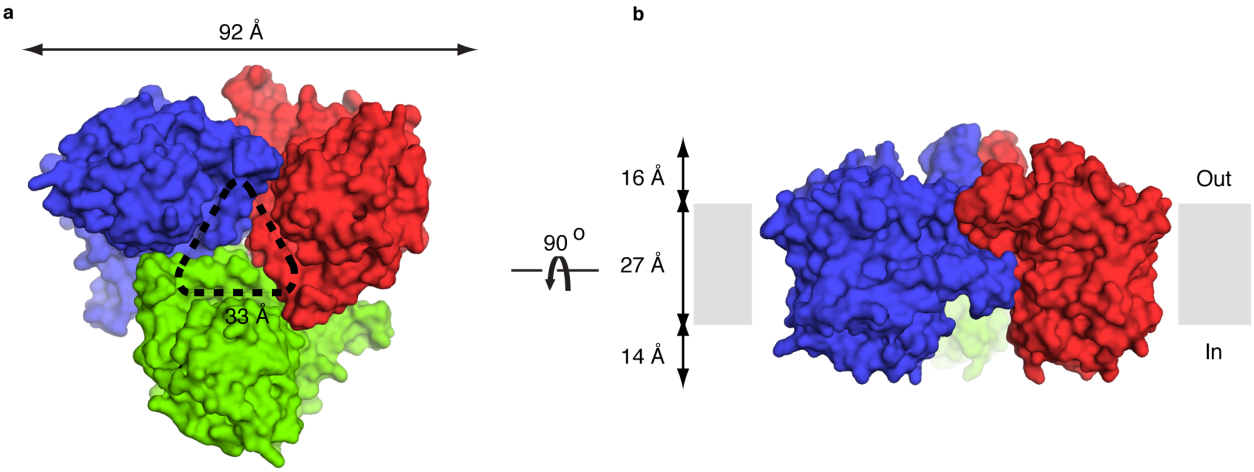

Supplementary Figure 3. Trimeric structure of vcCNT. (**a**) Surface representations for the vcCNT trimer viewed from the cytoplasm. Individual protomers are colored blue, red, and green. (**b**) Surface representations for the vcCNT trimer viewed parallel to the membrane. The putative membrane bilayer is indicated in **b** with grey boxes. The dimensions of the putative membrane bilayer, extracellular region, and intracellular region are shown.

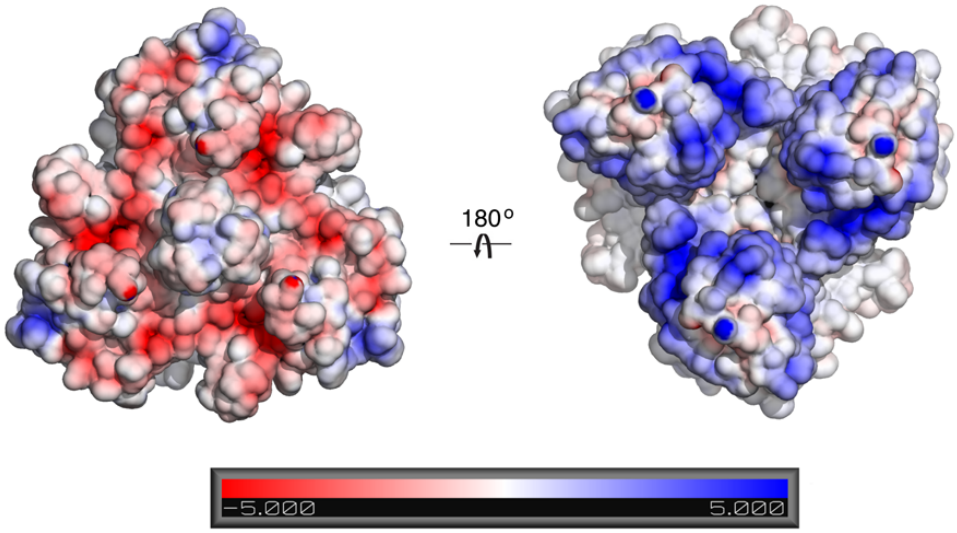

Supplementary Figure 4. An electrostatic surface representation of vcCNT was calculated from -5 kT (negatively charged amino acids) to 5 kT (positively charged amino acids) using the program the Adaptive Poisson-Boltzmann Solver (APBS) [3]. The view of the trimer from the extracellular side is shown on the left and the view of the trimer from the intracellular side is shown on the right. The localization of positively charged residues on the intracellular side and negatively charged residues on the extracellular side shows that the structure conforms to the positive-inside rule.

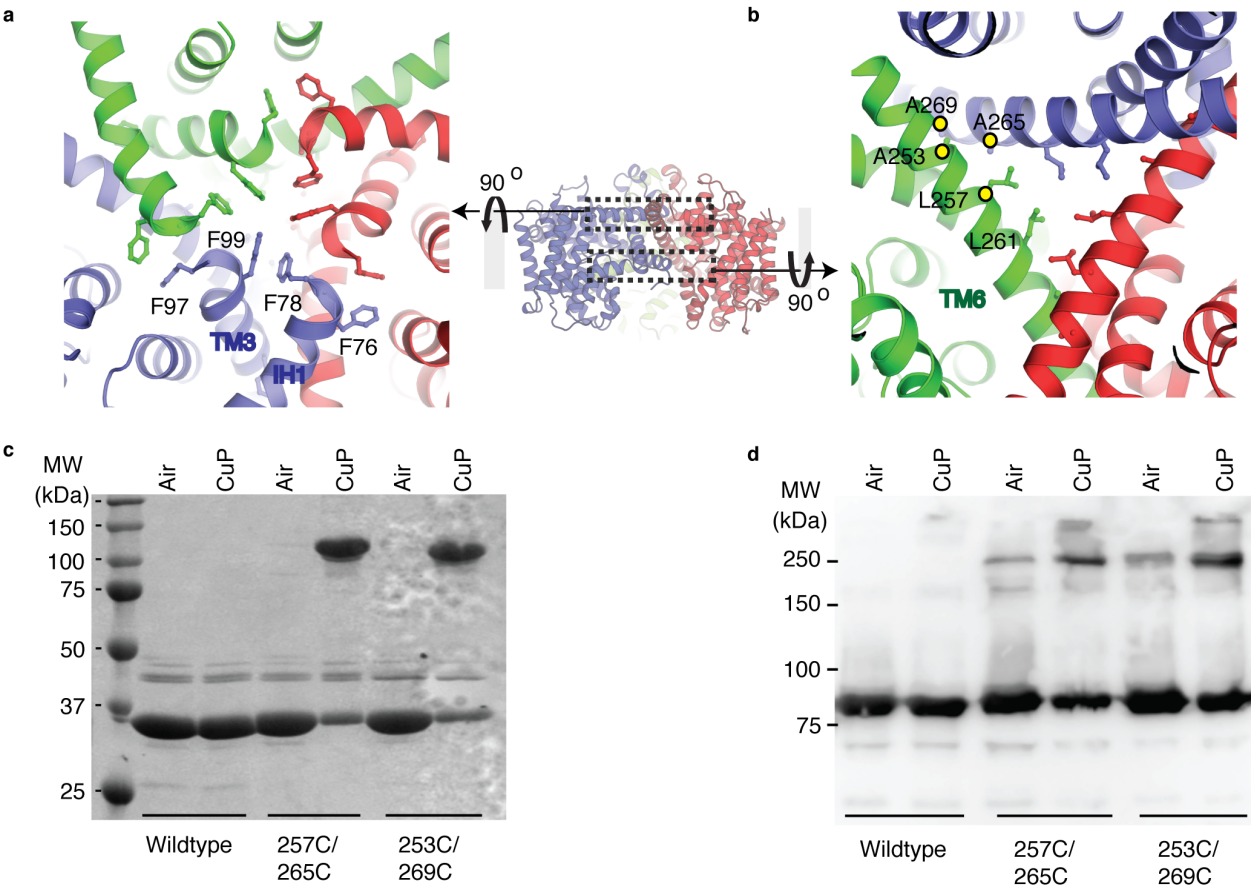

Supplementary Figure 5. Trimer interface and oligomeric state of vcCNT. **a**, The trimer interface at the outer leaflet of the membrane viewed from the extracellular side. The protomers are colored blue, red, and green. **b**, The trimer interface at the inner leaflet of the membrane viewed from the intracellular side. Residues mutated to Cys for cross-linking experiments are denoted with yellow circles. **c**, Coomassie-stained SDS-PAGE analysis of cross-linking. Wildtype, 253C/269C, and 257C/265C in detergent micelles are untreated and treated with 50 μM copper phenanthroline. **d**, Western blot analysis of cross-linking. Cell membranes containing maltose-binding protein (MBP) fused vcCNT (wildtype), MBP-vcCNT (253C/269C), and MBP-vcCNT (257C/265C) were untreated and treated with 50 μM copper phenanthroline. MBP does not contain any endogenous cysteines. Molecular weight markers are indicated on the left in **c** and **d**.

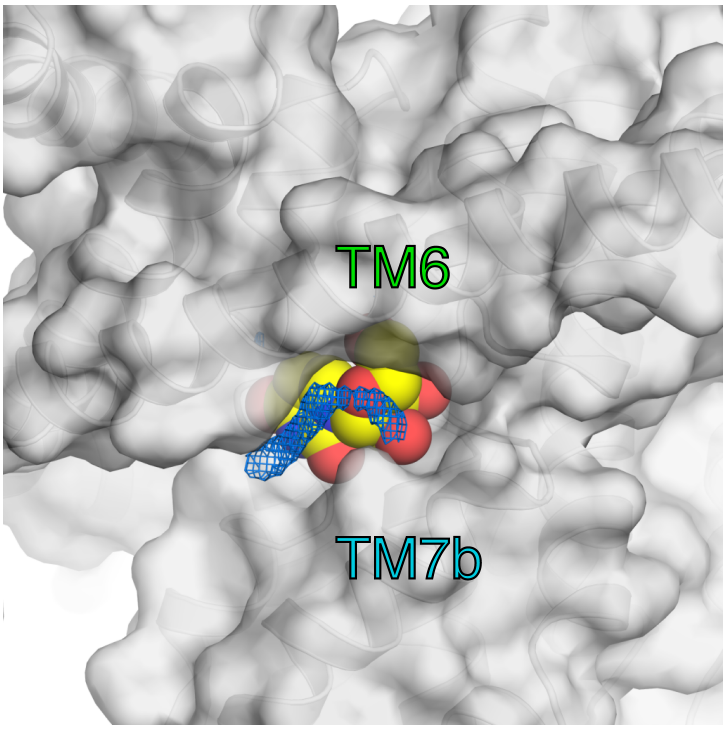

Supplementary Figure 6. Surface representation of vcCNT zoomed in on the nucleoside-binding site with a similar viewpoint as that of Figure 3c. Uridine is shown as spheres. TM6 and TM7b partly cover the binding site therefore uridine is not free to be released into the intracellular solution. The blue mesh, blocking the crevice between TM6 and TM7b, is from an Fo-Fc OMIT map contoured at 3 σ. The observed elongated density peak may correspond to an acyl chain from either a lipid or a detergent molecule which may further block the release of uridine into the intracellular basin.

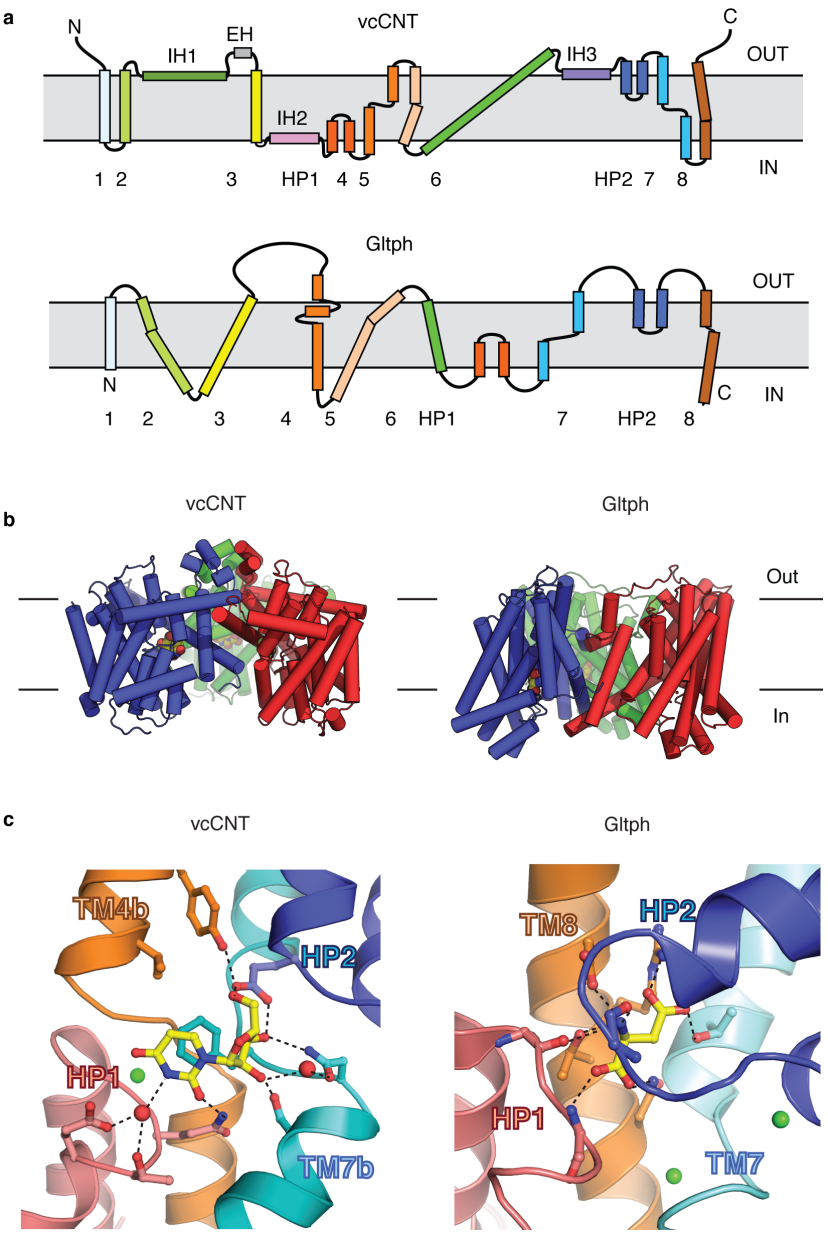

Supplementary Figure 7. Comparison of vcCNT with Glt_{Ph}. **a,** Topology of vcCNT and Glt_{Ph}. Helices are colored as in Figures 3 and 5. **b,** Trimer architecture of vcCNT and Glt_{Ph}. Individual protomers are colored differently and substrates (uridine and glutamate, respectively) are shown as spheres. **c,** Substrate binding sites of vcCNT and Glt_{Ph}. Hydrogen bonds are shown as dashed lines. Sodium ions are shown as green spheres and water molecules are shown as red spheres.

Supplementary Discussion

1. Hypothetical model of nucleoside transport by vcCNT

In hCNT3, Glu 343 (Glu 156 in vcCNT) and Glu 519 (Glu 332 in vcCNT) are accessible to the extracellular solution when mutated to cysteines [4]. In our structure, the corresponding residues are located closer to the intracellular side and interact with uridine (Figure 3a and 3c in the main text). The accessibility data strongly suggest that these nucleoside-binding residues must be accessible to the extracellular milieu to capture nucleosides during the transport cycle. Inspection of the crystal structure reveals that the interactions between TM6 and HP2 form a hydrophobic seal that blocks access to the nucleoside-binding pocket from the extracellular side (Figure 3b and Figure 4). If the nucleoside-binding site relocates slightly above TM6, it will be readily accessible to the extracellular side, suggesting that TM6 serves as a hydrophobic barrier for nucleoside transport. In forming a hypothesis for the conformational change that mediates the motion of the nucleoside-binding pocket, we looked to the structural studies of Glt_{Ph} [5,6]. Although many differences exist between vcCNT and Glt_{Ph} such as opposite topologies and different folds, the commonalities of using two helical hairpins and an unwound helix (two unwound helices for vcCNT) for substrate and sodium binding suggest that there is a shared mechanism of substrate transport between these two different classes of transporters. In Glt_{Ph} HP1, HP2, and part of TM7 and TM8, which form the substrate-binding site, move across the membrane bilayer by way of a rigid-body motion (Supplementary Figure 7) [5]. We speculate that a similar rigid-body motion of HP1, HP2, and other parts of the transport domain (probably TM4 and TM7) is responsible for the transition from an inward-facing state to an outward-facing state (Figure 7). Since only TM6 serves as a hydrophobic barrier to cross, relatively smaller motion (~10 Å) is required for nucleoside transport by vcCNT compared to that of Glt_{Ph} [5]. We do not

know whether part of the transport domain or the entire transport domain moves, as the composition of the transport domain and the connections between the transport domain and scaffold domain are different between Glt_{Ph} and vcCNT.

2. Comparison with Glt_{Ph}

Even though vcCNT adopts a novel fold, a couple of structural features are reminiscent of the structure of the glutamate transporter Glt_{Ph} such as trimeric subunit stoichimetry and usage of two helical hairpins for substrate binding. Since Glt_{Ph} is one of the well-studied secondary transporter systems, we compared our structure with that of Glt_{Ph} to gain insight into the mechanism of our transporter.

The topology of vcCNT is opposite that of Glt_{Ph}: vcCNT has both N- and C-termini located on the extracellular side while Glt_{Ph} has both N- and C-termini located on the intracellular side. Although the topologies and overall folds of Glt_{Ph} and vcCNT are quite different (Supplementary Figures 6a and 6b), both Glt_{Ph} and vcCNT share a similar design principle: a scaffold domain (termed trimerization domain for Glt_{Ph}) that is located at the outermost layer of the transporter and a transport domain that is located inside the scaffold domain. In Glt_{Ph}, the two domains are separated in sequence: the scaffold domain is composed of the N-terminal half (TM1-TM6) and the transport domain is composed of the C-terminal half (HP1 - TM8). In vcCNT, the two domains are not (TM1, TM2, IH1, and TM6 for the scaffold domain).

With regard to the scaffold (trimerization) domain, it is difficult to find any commonalities between vcCNT and Glt_{Ph} in terms of folds and the way trimerization is achieved. With regard to the transport domain, the noticeable differences are in the arrangement of the substrate-binding site and the location of the Na^+-binding site (Supplementary figure 7c). In Glt_{Ph}, HP1, HP2,

unwound TM7, and TM8 line the substrate-binding site. The substrate interacts mostly with TM8 (corresponding to TM4 in vcCNT) and HP2 covers the substrate to isolate it from the extracellular and intracellular sides. In other words, the occluded state is mediated by HP2. In vcCNT, HP1, HP2, unwound TM4 (corresponding to TM8 in Glt_{Ph}), and unwound TM7 (corresponding to TM7 in Glt_{Ph}) line the substrate binding site. The interactions with the substrate are spread out through the tips of the two HPs and unwound regions of TM7. TM6 covers the substrate partly (instead of HP2 in Glt_{Ph}) thereby preventing the release of the substrate into the intracellular side. Since most of the substrate binding is mediated by HP1 and HP2, it is unlikely that either HP1 or HP2 rearranges to cover the substrate to provide an occluded state in vcCNT. Most likely the occluded state is provided by TM6 in vcCNT. In Glt_{Ph}, one sodium-binding site is localized between HP2 and the unwound region of TM7 and the other sodium-binding site is localized between TM7a and TM8 (Supplementary Figure 6c). In contrast, the sodium-binding site observed in vcCNT is localized between HP1 and TM4b (TM8 in Glt_{Ph}). Given these differences, we propose that the detailed mechanism of sodium coupling and occlusion are significantly different between Glt_{Ph} and vcCNT although the overall mechanism of substrate transport via alternating access is similar.

In the field of secondary active transporters, the dominating structural fold is that of LeuT: the five-helix inverted repeat motif [7-12]. Now we have observed that helical hairpins and unwound helices are utilized for substrate binding in transporters sharing different overall folds, which may be more common for secondary active transporters than was once thought [13].

3. Oligomerization state

The crystal structure suggests that vcCNT adopts a trimeric configuration. The center of the trimer is sealed off with hydrophobic amino acids at both the extracellular and intracellular sides of the membrane so it is therefore unlikely that nucleosides or Na^+ ions permeate through the trimerization interface (Supplementary Figure 5a).

Inspection of the interface reveals that the trimer contacts are mediated by conserved amino acids from the C-terminal part of IH1, EH, TM3, and TM6 and cover an area of ~1200 $Å^2$ per protomer. At the extracelluar side, the trimer interface is mainly composed of interactions among conserved phenylalanines from the N-terminal part of TM3 (Phe 97 and Phe 99) and from the C-terminal part of IH1 (Phe 76 and Phe 78) (Supplementary Figure 5a). At the intracellular side, TM6 forms an interface that seals off the trimer axis by van der Waals interactions among conserved hydrophobic amino acids. EH, a short stretch of helices protruding into the extracellular solution, forms a part of the interface by hydrophobic interactions but the sequence of EH is not conserved and this feature is only an insertion unique to vcCNT (Supplementary Figure 1).

To test whether the stoichiometry of vcCNT is trimeric and further validate the physiological relevancy of our crystal structure, we have performed disulfide bridge cross-linking experiments. Based on the crystal structure, we designed two double cysteine mutants (referred to as L257C/A265C and A253C/A269C, respectively) with the mutated cysteines positioned at the trimer interface (Supplementary Figure 5b). Addition of the oxidant copper 1,10-phenanthroline to the double mutants in both detergent micelles and isolated *E. coli* membranes causes trimer formation as judged by the generation of a new band that migrates at the expected trimer size when subjected to gel electrophoresis (Supplementary Figure 5c and 5d). Since our structure-based cysteine mutants readily form disulfide bridge cross-linked trimers in both detergent

micelles and cell membranes, our crystal structure reflects a physiologically relevant structure and oligomerization state. Given the sequence conservation of most of the amino acids involved in trimerization, we propose that the stoichiometry of both eukaryotic and prokaryotic CNT family members is trimeric (Supplementary Figure 1).

References:

1 Slugoski, M. D. *et al.* Substituted cysteine accessibility method analysis of human concentrative nucleoside transporter hCNT3 reveals a novel discontinuous region of functional importance within the CNT family motif (G/A)XKX3NEFVA(Y/M/F). *J Biol Chem* **284**, 17281-17292, doi:M109.009704 (2009).

2 Hamilton, S. R. *et al.* Subcellular distribution and membrane topology of the mammalian concentrative Na+-nucleoside cotransporter rCNT1. *J Biol Chem* **276**, 27981-27988, doi:10.1074/jbc.M100518200 (2001).

3 Baker, N. A., Sept, D., Joseph, S., Holst, M. J. & McCammon, J. A. Electrostatics of nanosystems: application to microtubules and the ribosome. *Proc Natl Acad Sci U S A* **98**, 10037-10041, doi:10.1073/pnas.181342398 (2001).

4 Slugoski, M. D. *et al.* Conserved glutamate residues Glu-343 and Glu-519 provide mechanistic insights into cation/nucleoside cotransport by human concentrative nucleoside transporter hCNT3. *J Biol Chem* **284**, 17266-17280, doi:M109.009613 (2009).

5 Reyes, N., Ginter, C. & Boudker, O. Transport mechanism of a bacterial homologue of glutamate transporters. *Nature* **462**, 880-885, doi:nature08616 (2009).

6 Yernool, D., Boudker, O., Jin, Y. & Gouaux, E. Structure of a glutamate transporter homologue from Pyrococcus horikoshii. *Nature* **431**, 811-818, doi:nature03018 (2004).

7 Fang, Y. *et al.* Structure of a prokaryotic virtual proton pump at 3.2 A resolution. *Nature* **460**, 1040-1043, doi:nature08201 (2009).

8 Gao, X. *et al.* Structure and mechanism of an amino acid antiporter. *Science* **324**, 1565-1568, doi:1173654 (2009).

9 Ressl, S., Terwisscha van Scheltinga, A. C., Vonrhein, C., Ott, V. & Ziegler, C. Molecular basis of transport and regulation in the Na(+)/betaine symporter BetP. *Nature* **458**, 47-52, doi:nature07819 (2009).

10 Shaffer, P. L., Goehring, A., Shankaranarayanan, A. & Gouaux, E. Structure and mechanism of a Na+-independent amino acid transporter. *Science* **325**, 1010-1014, doi:1176088 (2009).

11 Weyand, S. *et al.* Structure and molecular mechanism of a nucleobase-cation-symport-1 family transporter. *Science* **322**, 709-713, doi:1164440 (2008).

12 Yamashita, A., Singh, S. K., Kawate, T., Jin, Y. & Gouaux, E. Crystal structure of a bacterial homologue of Na+/Cl--dependent neurotransmitter transporters. *Nature* **437**, 215-223, doi:nature03978 (2005).

13 Krishnamurthy, H., Piscitelli, C. L. & Gouaux, E. Unlocking the molecular secrets of sodium-coupled transporters. *Nature* **459**, 347-355, doi:nature08143 [pii] 10.1038/nature08143 (2009).